Extended Data Figs.

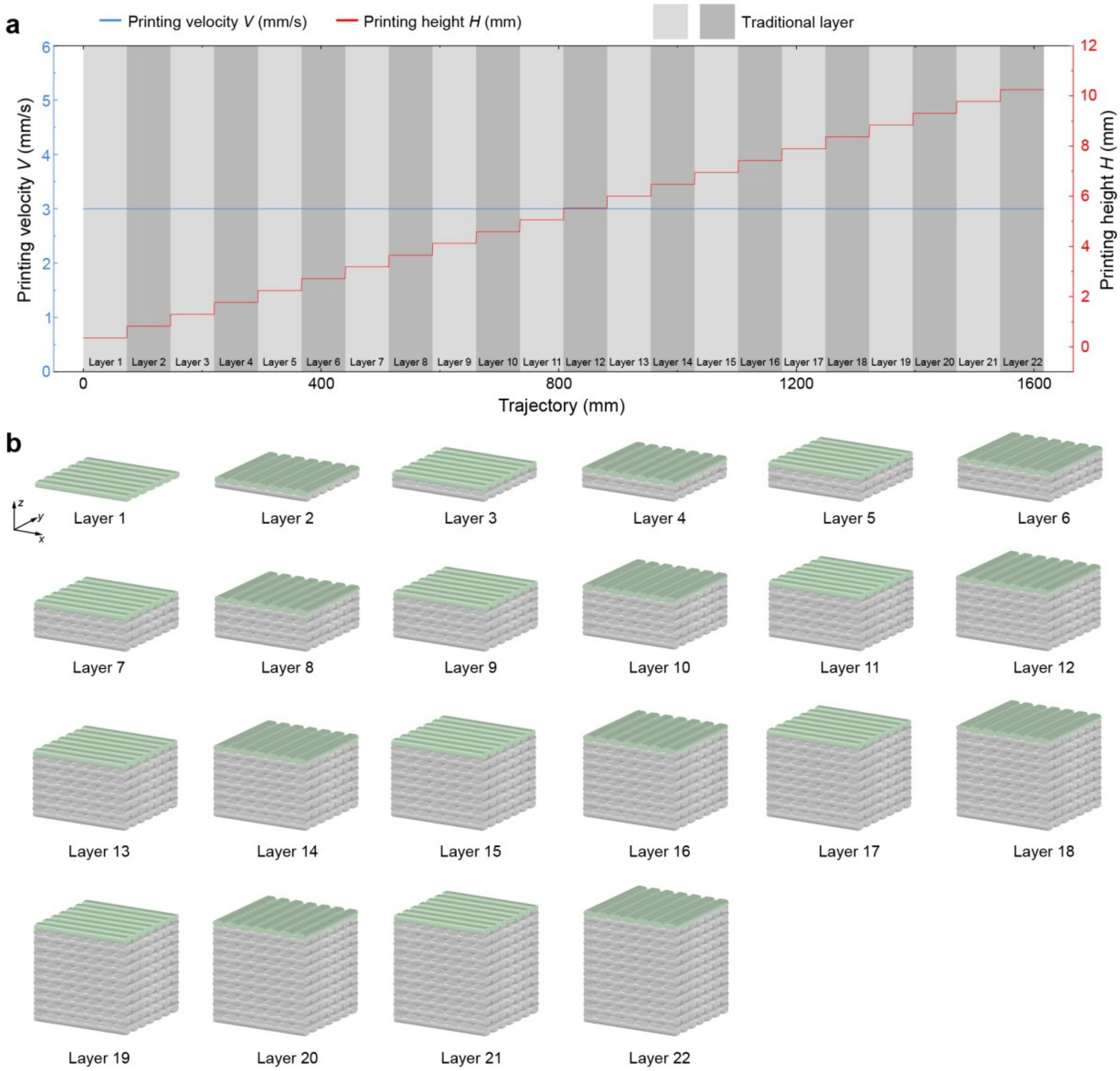

Extended Data Fig. 1 | Phase diagram of printing parameters and filament stacking models of homogeneous porous sample created via traditional-3DP strategy. a, Details of V and H. V and H are fixed during the intra-layer printing process. H is the distance from the nozzle outlet to the substrate. The difference between H and h are shown in **Supplementary Figure 1**. **b**, A series of uniform pore models with constant D and cross-sectional shape (width l_w and height l_h). The final model was constructed by stacking 22-layer filaments.

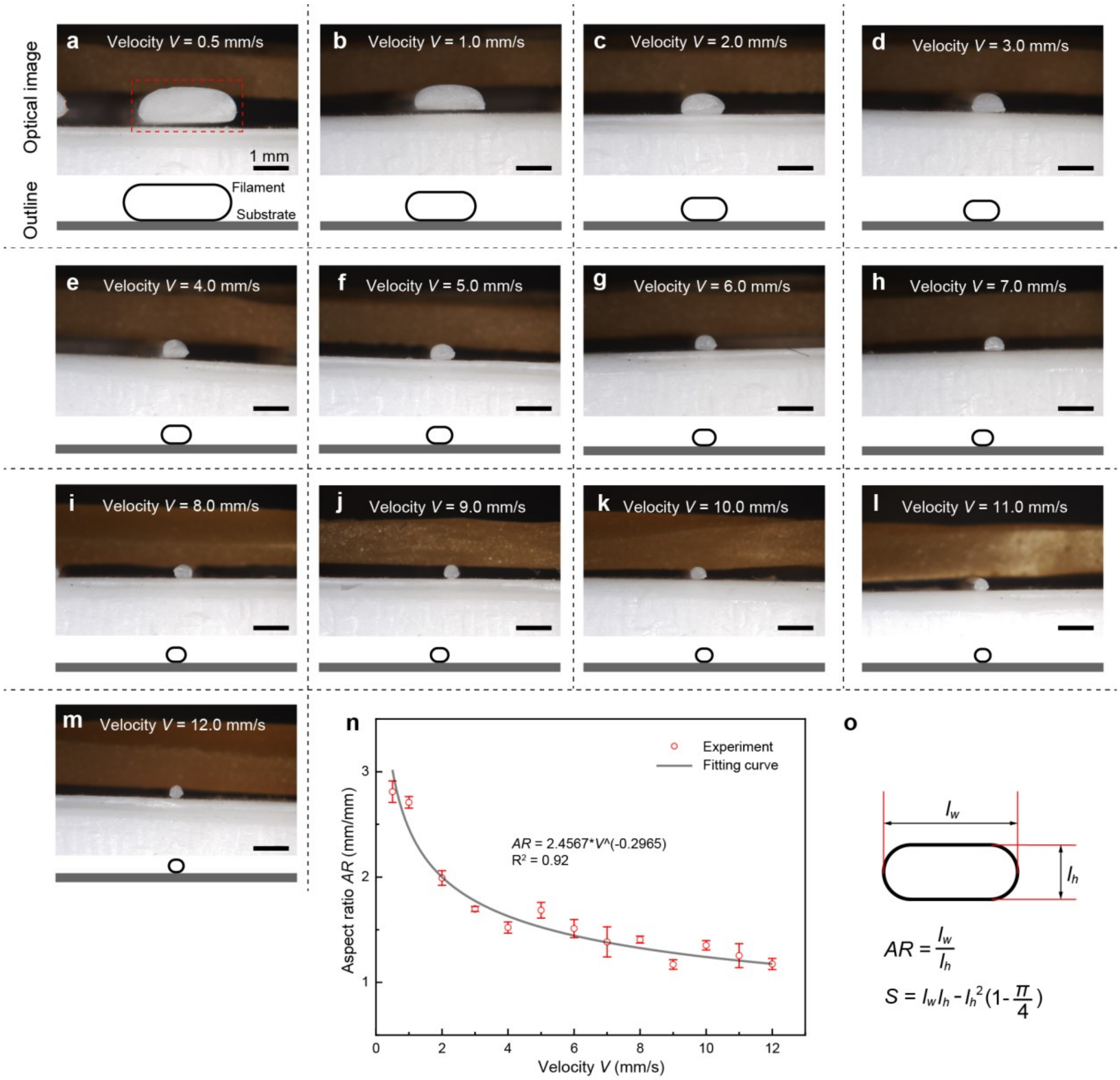

Extended Data Fig. 2 | Filament cross-sections at different printing velocities *V* (a-m), relationship between printing velocity *V* and aspect ratio *AR* (n), and schematic diagram of oblong filament cross section (o). *AR* gradually decreases as the printing velocity *V* increases. Data is mean ± standard error (means ± s.d., n = 4). The filament cross-section is nearly oblong, and its key parameters are cross-sectional width l_w and height l_h. The following functions can be obtained: aspect ratio $AR = l_w/l_h$ and cross-sectional area $S = l_w \times l_h - l_h^2(1-\pi/4)$.

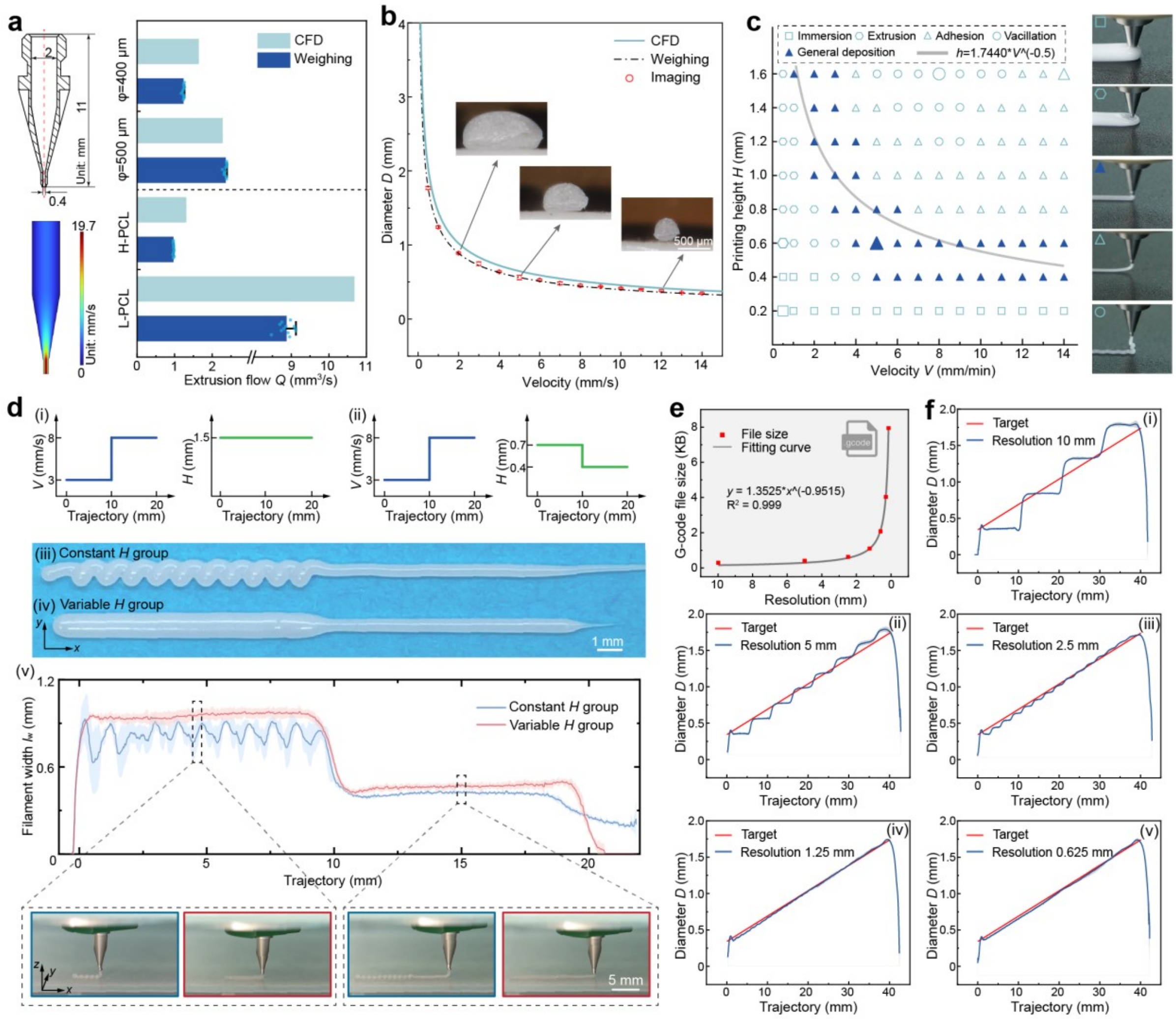

Extended Data Fig. 3 | Key parameters of the FDA-3DP strategy. a, Simulation and experiment for extrusion flow rate Q. The nozzle inner diameter φ = 400 and 500 μm groups were implemented using H-PCL material (mean ± s.d., n = 8). The H-PCL and L-PCL groups were employed using nozzle inner diameter φ = 400 μm (mean ± s.d., n = 8). The computational fluid dynamics (CFD) cloud is the simulation result at a nozzle inner diameter of φ = 400 μm, a material of H-PCL, and an extrusion pressure of 400 kPa (detailed CFD results see **Supplementary Figure 4**). **b**, Results of CFD, weighing, and imaging simulated D at different V. (mean ± s.d., n = 4). The CFD and weighing results are from (**a**) (φ = 400 μm and H-PCL material). **c**, Map of the effect of V and H on filament deposition states (**Supplementary Figure 5**). Enlarged symbols on the left correspond to the deposition states on the right. The solid triangles are an acceptable deposition state, and are fitted to obtain a function of $H = 1.744 \times V^{-0.5}$. **d**, Showing the ability of our proposed strategy to maintain the filament deposition state. (i) and (ii) demonstrate the V and H settings of the constant and variable H groups on a 40 mm-long filament, respectively. (iii) and (iv) illustrate the top views of printed filaments. (v) the upper figure quantitatively evaluates the filament deposition state by the filament cross-section width l_w using software ImageJ (mean ± s.d., n = 4) (see processing details in **Extended Data Fig. 4**), and the lower figure shows the keyframes of the filament deposition during printing (frames captured from **Supplementary Videos 2-3**). **e**, Plotting of fabrication resolution and corresponding G-code file size. **f**, Design (target) and experimental results of variable *D* at fabrication resolution of 10, 5, 2.5, 1.25, and 0.625 mm (mean ± s.d., n = 4).

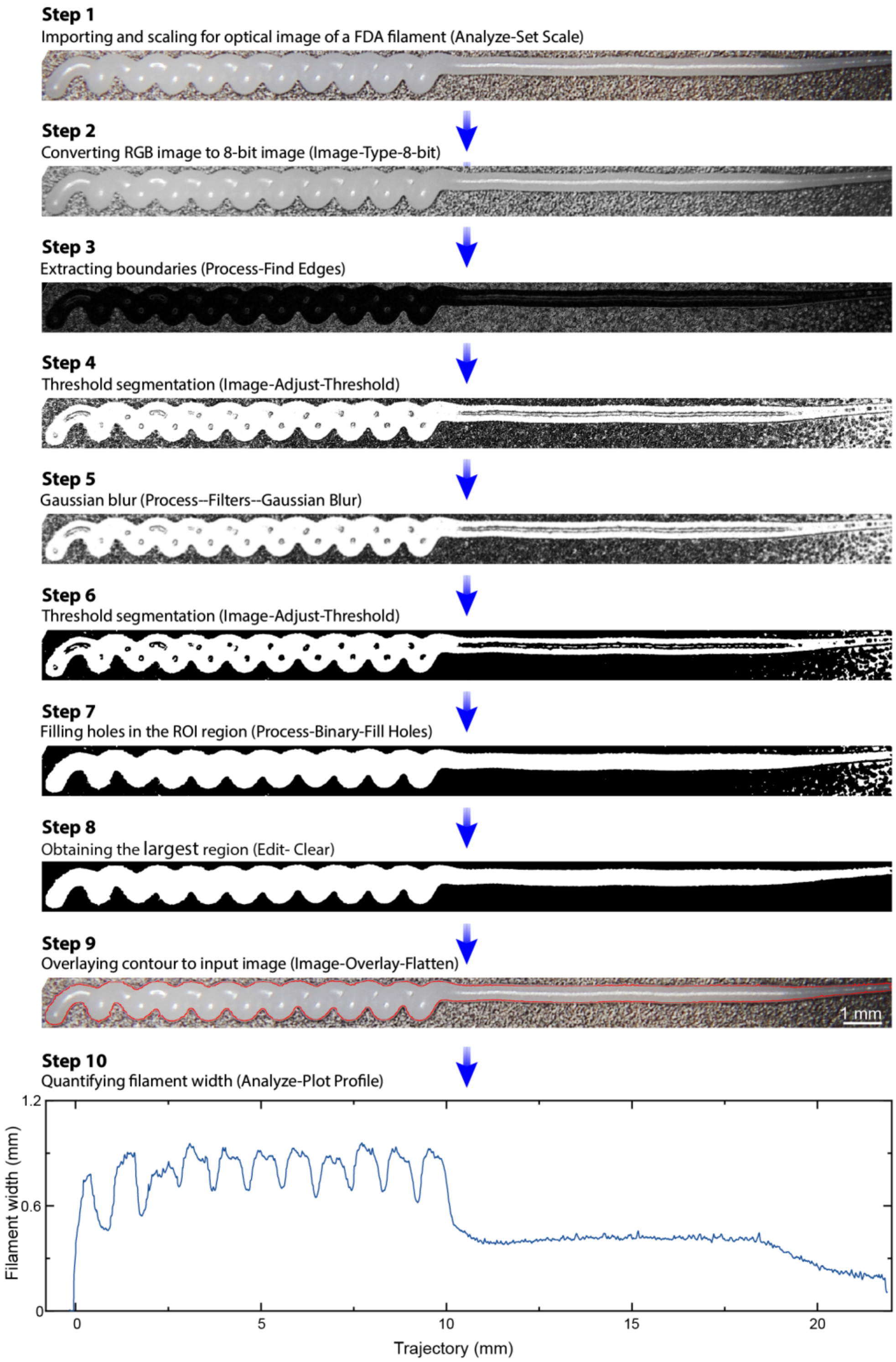

Extended Data Fig. 4 | Steps for quantifying filament width l_w using software ImageJ.

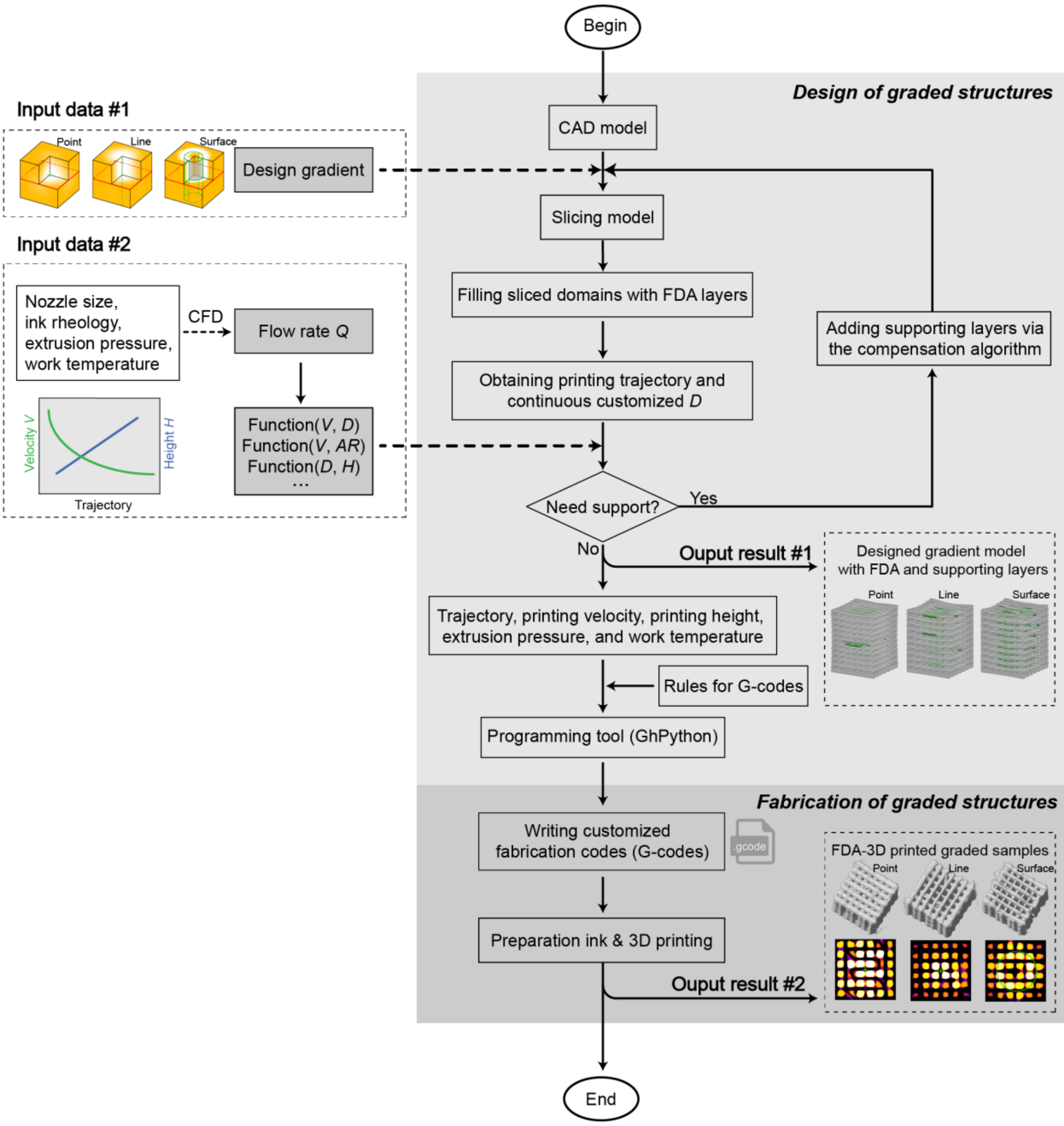

Extended Data Fig. 5 | Overview of design and fabrication of gradient pore structures based on the FDA-3DP strategy. Input data #1, design gradient of pore size; input data #2, printing conditions and mathematical functions (equations (1) and **Supplementary Note 4**). Output result #1, designed 3D model with FDA and supporting layers; output result #2, FDA-3D printed samples. Extrusion flow rate, *Q*; printing velocity, *V*; printing height *H*; ideal filament diameter, *D*; aspect ratio, *AR*; and computational fluid dynamics, CFD.

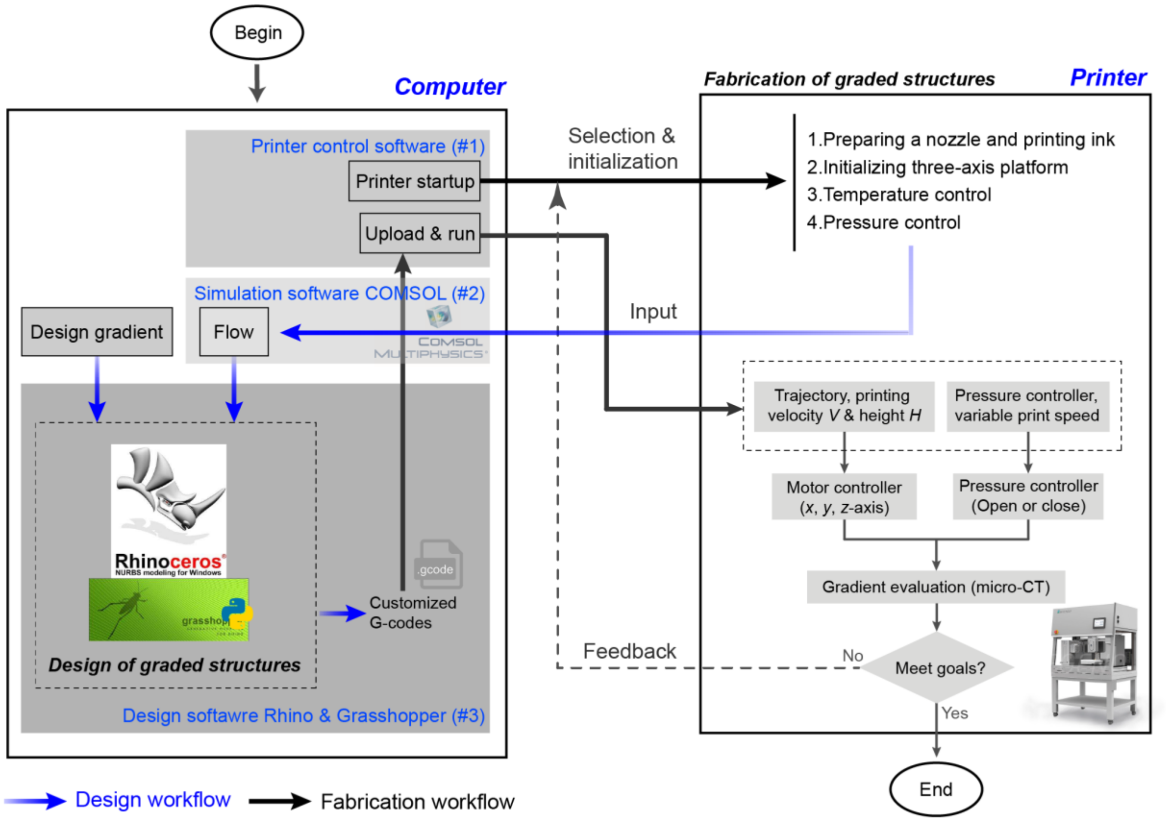

Extended Data Fig. 6 | Workflow between computer and printer in the FDA-3DP strategy.

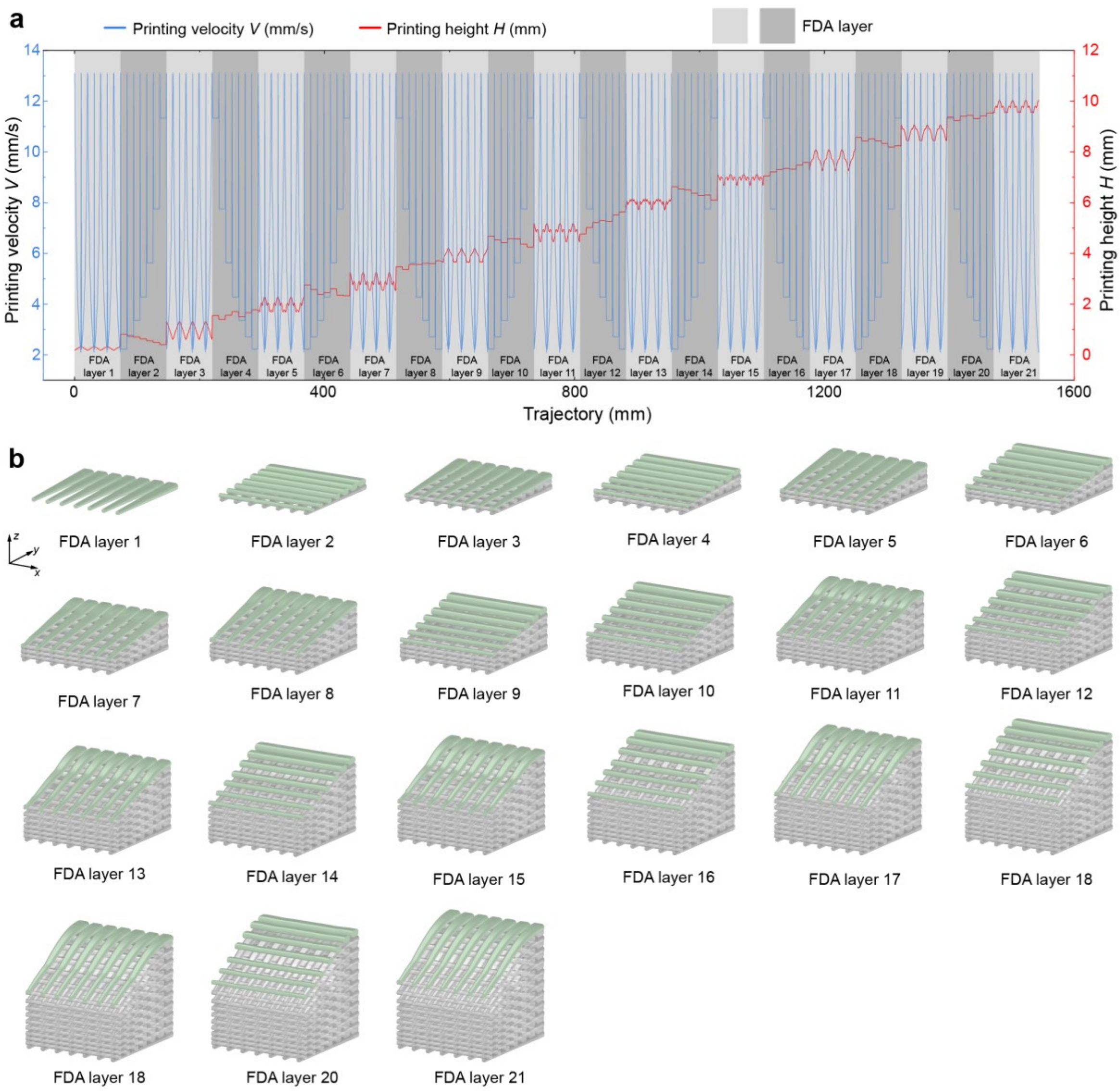

Extended Data Fig. 7 | Phase diagram of printing parameters and filament stacking models of the horizontal gradient model without supporting layers created by FDA-3DP strategy. a, Details of *V* and *H*. During printing, *V* and *H* are continuously changed to precisely control the volume of deposited ink on the printing trajectory. **b**, A series of horizontal gradient pore models with variable-*D* FDA layers. The final model was constructed by stacking 21-layer filaments.

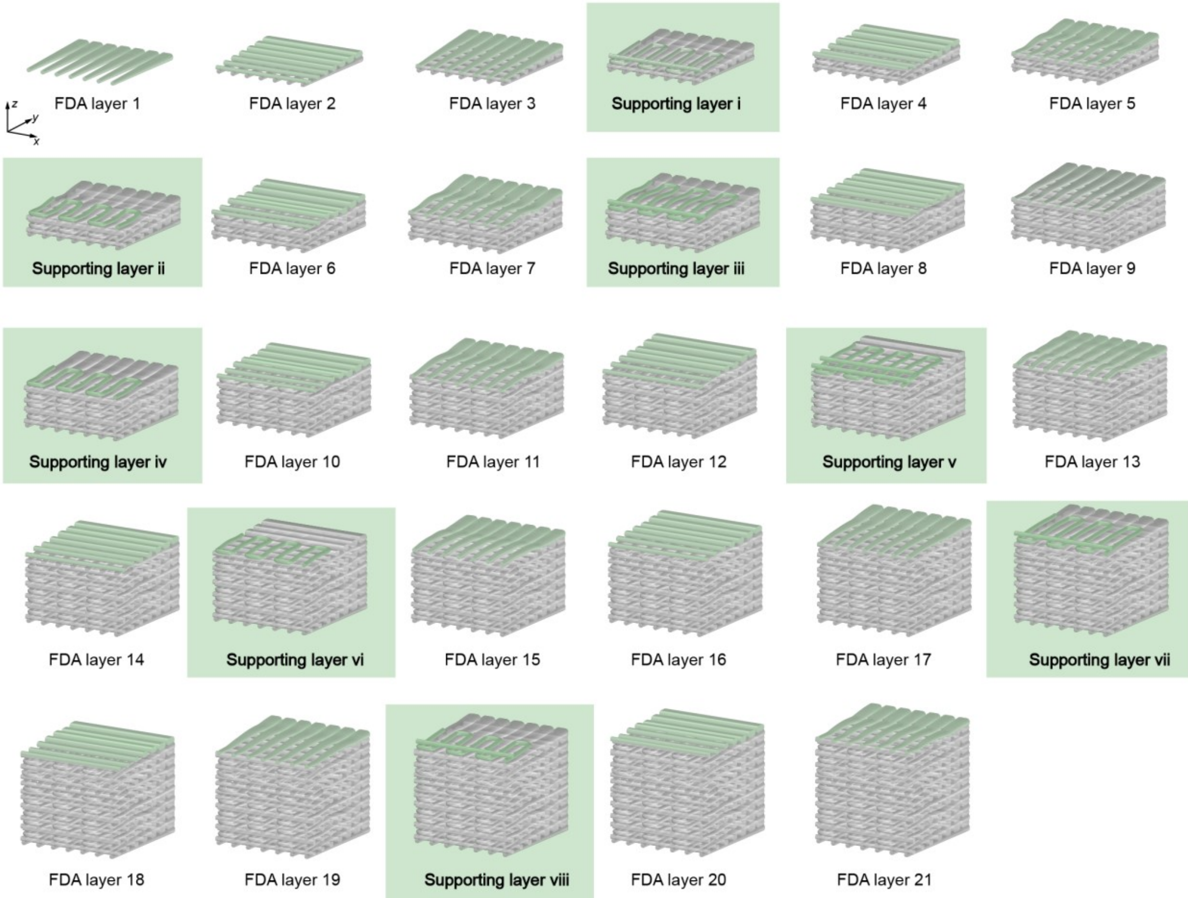

Extended Data Fig. 8 | Filament stacking models of the horizontal gradient pore model with FDA and supporting layers created by FDA-3DP strategy. A series of horizontal gradient pore models with variable-*D* FDA layers and constant-*D* supporting layers. The final model without collapse region was constructed by stacking 21-layer FDA filaments and 8-layer supporting filaments.

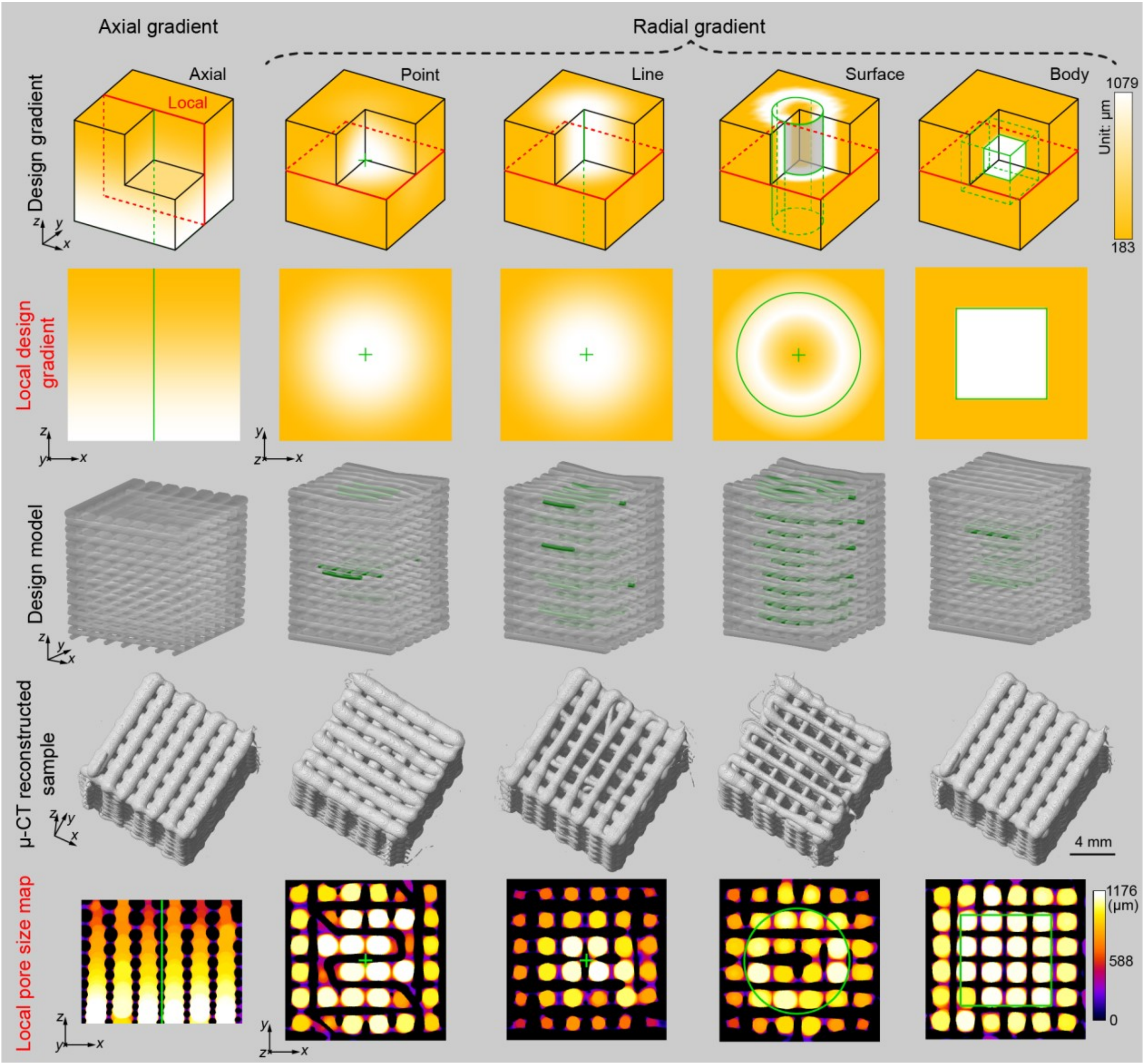

Extended Data Fig. 9 | Design, fabrication, and evaluation of axial and radial gradient pore structures. The detailed design and printing parameters of the axial and radial gradient pore structures are shown in **Supplementary Table 2**. To demonstrate the internal gradient pore, the vertical and horizontal planes (enclosed by red lines, see Design gradient) are selected as local regions of interest for the axial and radial gradients, respectively. The designed 3D models were obtained based on our proposed FDA-3DP strategy using the software Rhino and its embedded parametric tool Grasshopper. Pore size maps are evaluated quantitatively by software ImageJ (full series of 2D images along z-axis, see **Supplementary Video 5**), where the black and colored areas are the sample material and the pore structure, respectively.

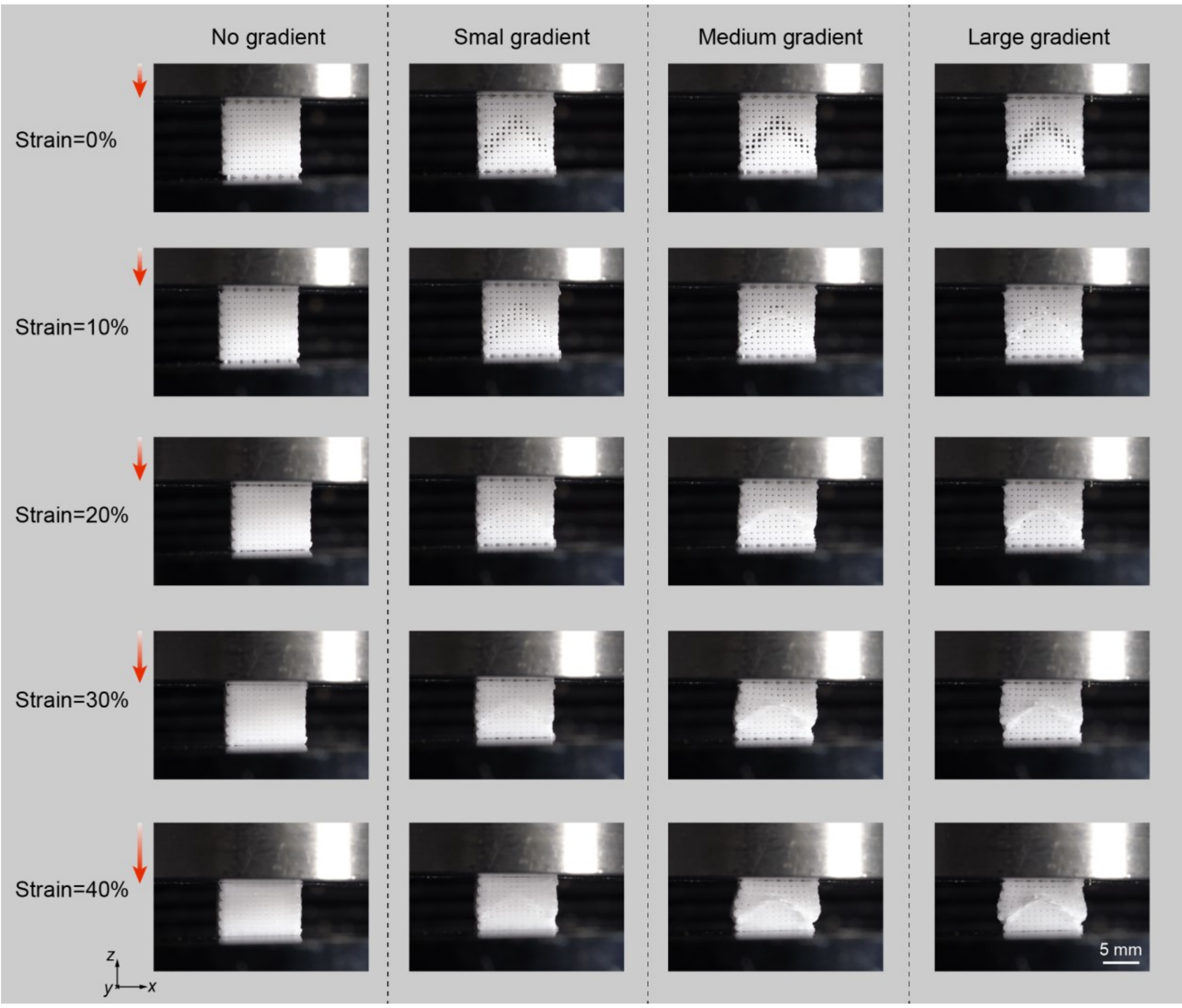

Extended Data Fig. 10 | Deformation of four samples with embedded V letter in uniaxial compression from 0% to 40% strain. The no gradient group do not have predictable regions of deformation during the compression process. Within ~20% strain, the V region of the three gradient groups is squeezed and the non-V region is not squeezed; after ~20% strain, the non-V region starts to be squeezed.